DTU Library

Ship-Iceberg Detection & Classification in Sentinel-1 SAR Images

Heiselberg, H.

Link back to DTU Orbit

Ship-Iceberg Detection & Classification in Sentinel-1 SAR Images

H. Heiselberg

National Space Institute, Technical University of Denmark, 2800 Kongens Lyngby, Denmark.

(e-mail: hh@dtu.dk).

Abstract—**The European Space Agency Sentinel-1 satellites provide good resolution all weather SAR images. We describe algorithms for detection and classification of ships, icebergs and other objects at sea. Sidelobes from strongly reflecting objects as large ships are suppressed for better determination of ship parameters. The resulting improved ship lengths and breadths are larger than the ground truth values known from Automatic Identification System (AIS) data due to the limited resolution in the processing of the SAR images as compared to previous analyses of Sentinel-2 optical images. The limited resolution in SAR imagery degrades spatial classification algorithms but it is found that the backscatter horizontal and vertical polarizations can be exploited to distinguish icebergs in the Arctic from large ships but not small boats or wakes.**

Index Terms—**Sentinel-1, SAR, ship detection, ship lengths, icebergs**

I. INTRODUCTION

MARINE surveillance and situation awareness is essential for monitoring and controlling piracy, smuggling, fishing, irregular migration, trespassing, spying, traffic safety, icebergs, sea ice, shipwrecks, the environment (oil spill or pollution), etc. *Dark ships* are non-cooperative ships with non-functioning transponder systems such as the automatic identification system (AIS). Their transmission may be jammed, spoofed, sometimes experience erroneous returns, or simply turned off deliberately or by accident. Furthermore, AIS satellite coverage at high latitudes is sparse, which means that other non-cooperative surveillance systems, including satellite or airborne systems, are required.

The Sentinel satellites under the Copernicus program [1] provide excellent and freely available imagery with pixel resolutions down to 10 m in multispectral and Synthetic Aperture Radar bands. The orbital periods are 6 days between the Sentinel-1 (S1) satellites A + B, and 5 days between the Sentinel-2 (S2) satellites A + B. Furthermore, the swaths from different satellite orbits overlap at higher latitudes, and the resulting frequent transits over the polar regions make these satellites particularly useful for Artic surveillance and for monitoring sea-ice coverage, icebergs and ships in SAR [2–11] and multispectral images (see [12-13] and refs. therein), etc.

Ship and iceberg detection in SAR imagery has recently been studied in detail for earlier satellites and TerraSAR-X [2-8] and Sentinel-1 [9-10]. Their different modes and resolutions lead to interesting differences for the ship detection lengths [5,6,10,11], classification in comparison to AIS and false alarm rates [2-11], etc. A comparison to these results will be made in the conclusion of this work.

In the following an analysis of the S1 SAR data and the search for objects in a sea background with masking of land and sea ice is presented. In addition, an algorithm for suppressing sidelobes from strongly reflecting objects as large ships is described, and a change detection algorithm which identifies stationary objects such as sea turbines, islands, piers, etc. Subsequently, the segment classification algorithm for ships and icebergs is described based on backscatter polarizations. Results for ships and icebergs in Denmark and Greenland are shown. Finally, ship lengths and breadths in S1 data are analysed and compared to AIS ground truth numbers. These results are also compared to earlier TerraSAR-X [4,5], S1 [9-10], Envisat [11], and S2 multispectral results [12-13].

II. SATELLITE IMAGES AND METHOD OF ANALYSIS

The S1 SAR images are analyzed using dedicated software developed specifically to optimize the classification of smaller ships and icebergs in large images.

A. Sentinel-1 SAR Images

S1 carries the C-band Synthetic Aperture Radar all-weather day-and-night imager [1]. As we are interested in small object classification and discrimination, we will focus on analyzing the processed level-1 high resolution ground range detected (GRDH) interferometric wide (IW) swath S1 images with 20x22m resolution, and pixel spacing l=10m. These are mega- to giga-pixel images with 16 bit grey levels. The titles above Figs. 1-5 are the filenames [1] that describes the data set (S1A-IW-GRD-polarization-date and time).

We analyze 30 S1 images covering several parts of Denmark and Greenland. These images are convenient for classification because objects are abundant and relatively easy to identify at sea. In Denmark the objects are ships, wind turbines, islands, and wakes whereas in Greenland there can be abundant icebergs and floes, some islands but few ships all depending on region, weather, time of year and day. The S1 images analyzed here are

recorded in 2018 from north of Denmark (Skagerak) down to the southeast and the Baltic Sea, and along the west coast of Greenland from Nuuk and up to the Disko Bay.
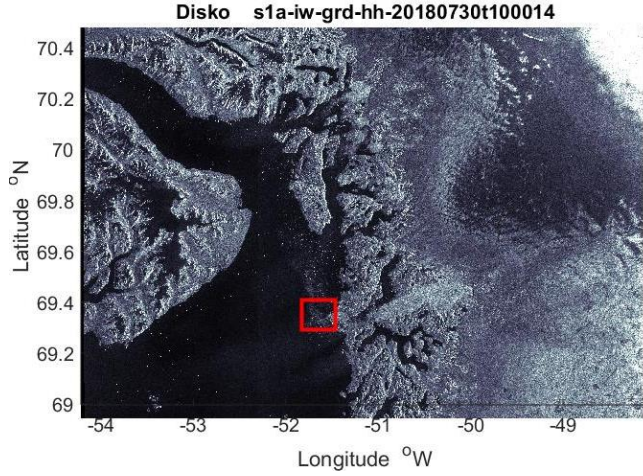

Fig. 1. The Disko Bay, Greenland. (July 30th, 2018, 10:00 a.m. UTC). The title is the filename (see text). The box is an iceberg ROI around the iceflow from the Ilulissat Icefjord, one of the worlds fastest flowing glaciers.
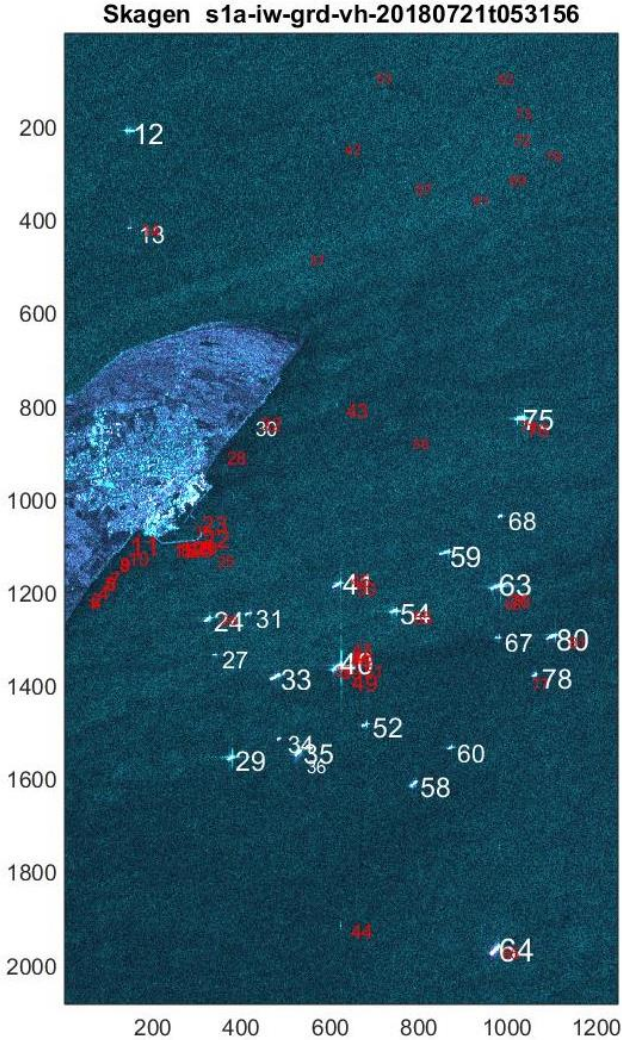

Fig. 2. Copernicus Sentinel-1A image [August 21st, 2018 at 05:32 a.m. UTC] covering Skagen, the northern tip of Denmark. The added numbers refer to the list of objects found by the classification algorithm, where white numbers are ships and red numbers are mostly wakes, sidelobes, and harbor piers.

The S1 images contain polarimetric SAR backscatter for horizontal (H) and vertical (V) polarizations transmitted and reflected. The dual direct polarized backscatter images are HH and HV in Arctic regions with abundant sea ice, but VV and VH in sub-Arctic regions because sea and wave reflect stronger in VV than in HH. The cross polarizations VH and HV are very similar.

The spatial coordinates (x,y) are the pixel coordinates (i,j) multiplied by the pixel resolution $l = 10$m for the S1 high resolution Ground Range Detected (GRDH) images. The total vertical backscatter is

$$V(i,j) = VH(i,j) + VV(i,j) , \qquad (1)$$

and analogously for the horizontal backscatter H=HH+HV. Examples are shown in Figs. 1-3.

B. Object detection from Background

To detect an object, its backscatter must deviate from the sea background which varies with satellite viewing (incidence) angle, wind and waves. Ship, ice, sea turbines, oil rigs, islands, and other objects generally reflect more. The next step is to select a region-of-interest (ROI) and mask large areas of land and sea ice by a simple algorithm which detects and connects segments [13] above a given area. Choosing the ROI such that the sea covers more than half of the image after land removal, the median backscatter value for each ROI image provides an accurate and robust value for the background. The detection threshold T_B is determined from the cumulative distribution for the ROI image such that the constant false alarm rate is 10^{-4}. If the ROI has megapixel size, this can lead to a large number of false alarms – mostly single pixels. Therefore, we filter objects larger than three pixels only, which effectively removes most false alarms from noise. The false alarm rate is at the same time sufficiently large that most if not all large and medium size ships are detected.

The total backscatter image V(i,j) or H(i,j) has the highest resolution and is therefore optimal for object search and detection. Treating these as matrices (see [13]), we construct a connectivity matrix in which pixels with total backscatter above and below the threshold T_B are assigned 1 and 0 respectively. In this connectivity matrix, all neighboring entries with value 1 are then connected as a *segment* (s), and listed $s = 1,..., N_s$, where N_s is the total number of separate segments found in the image. Each segment has an observed area corresponding to the sum over the pixels in the segment

$$A(s) = \sum_{i,j \in s}^{> T_B} 1 , \qquad (2)$$

in units of the pixel area (l^2). The cumulated backscatter of that segment is found by summing over its pixels

$$X(s) \ = \ \sum_{i,j \in s}^{> \ T_B} X(i,j) \ , \qquad (3)$$

for the co-polarized X=VV or HH, cross polarization X=VH or HV, or total backscatter X=V or H. We define the average backscatters

$$\bar{V}(s) \ = \ V(s)/A(s) , \quad \bar{H}(s) \ = \ H(s)/A(s) , \qquad (4)$$

and the cross polarization ratios

$$C_V(s) \ = \ VH(s)/V(s) \ , \quad C_H(s) \ = \ HV(s)/H(s) , \qquad (5)$$

which are very useful classifiers as will be shown below.
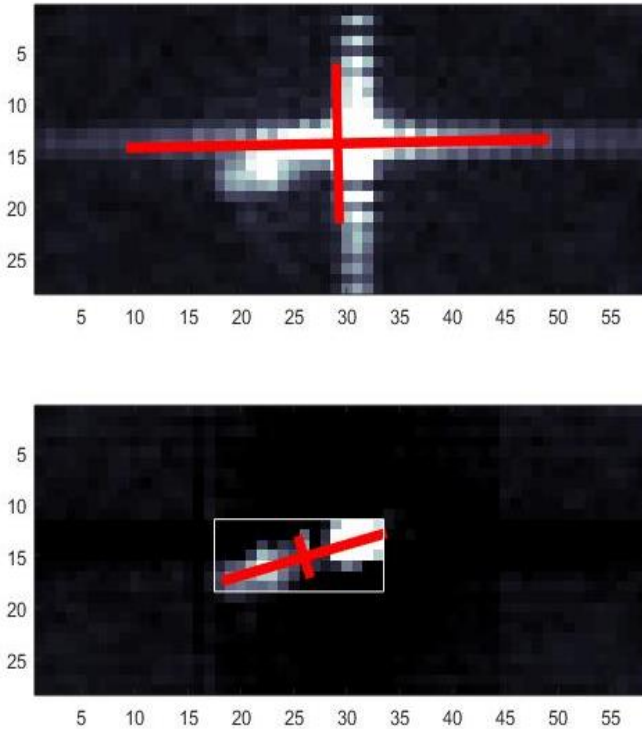

Fig. 3. Top: S1 SAR image of the container ship Ivar Reefer in Fig.2. Ship dimensions are 164x26m but show strong sidelobes. Bottom: sidelobes have been removed. Red bars show the resulting and improved ship length, breadth and direction.

C. Sidelobe removal

Sidelobes are often encountered in radar backscatter images. In particular ships and oil rigs, with large metal areas or corner reflectors can be very bright and produce strong sidelobes both along (*i*-direction) and transverse (*j*-direction) to the satellite swath direction. In Fig. 3 we show a typical SAR image of a container ship (Ivar Reefer) with strong sidelobes. These make classification difficult and corrupt the automatic determination of ship length, breadth and orientation. Therefore we apply a phenomenological correction algorithm which we have adjusted such that it effectively removes the sidelobes.

Whenever a pixel (i,j) value is so bright that it exceeds a sidelobe threshold T_S, the algorithm subtracts a value given by a simple sidelobe correction function

$$S_{ij}(i',j') \ = S_0 \ V(i,j) \ (\frac{\delta_{jj'}}{1 + | \ i' - i \ |/\lambda_i} + \frac{\delta_{ii'}}{1 + | \ j' - j \ |/\lambda_j}) \ , \qquad (6)$$

for pixels in the *x*-direction and *y*-direction separately relative to the bright pixel (i,j). The magnitude parameter $S_0=0.1$ is low such that the nearby pixels are not strongly suppressed such that the ship pixels remain, otherwise ships may be broken into separate segments. The sidelobe range parameters $\lambda_i = 10$ and $\lambda_j = 5$ are chosen such that the long range sidelobes are sufficiently suppressed. More precise modeling of the radiation pattern is difficult due to the finite pixel resolution, which is comparable to the oscillation length and implicitly the range parameters λ. They differ because the sidelobes in S1 images are stronger in the y-direction along swath. The Kronecker delta's $\delta_{ii'}$ and $\delta_{jj'}$ insure suppression of one row and one column respectively in the image matrix which cross at pixel (i,j). When several pixels (i,j) exceed the threshold, stripes are suppressed in the image as seen in Fig. 3.

The oscillating nature of sidelobes often leads to separate segments nearby a strongly reflecting object. Such "collaterals" are automatically picked up in the search and segment detection algorithm and can be classified as sidelobe remnant segments.

III. CLASSIFICATION

For all segments their position, length, width, area, total backscatter and cross polarization are calculated and listed. The classification scheme will as explained below identify the segment as an object such as a ship, iceberg or ice floe, wake, sidelobe, or a stationary object as an island, wind turbine, or oil rig. Each segment is assigned a number referring to a list with details on the calculated spatial and backscattering parameters. The numbers are plotted at the segment coordinates as shown in Fig. 2 with a color classification code.

A. Icebergs

Fig. 1 shows a S1 image from the Disko Bay in Greenland with thousands of icebergs and ice floes from several glaciers. As icebergs can come in many sizes and shapes, spatial parameters as area and length are not good classifiers. Instead the $\bar{H}$ and C_H classification parameters are useful for ice floe and iceberg classification as can be seen in Fig. 4. Most icebergs have low $\bar{H}$ and C_H, and are situated below the dashed line which therefore can be used for separating into classes by the k-nearest neighbor method.

B. Ships

Ships are identified from AIS ship coordinates and correlated with their positions in the satellite images. Fig. 2 shows a S1 image where a number of ships are anchored in the tranquil sea east of Skagen, the northern tip of Denmark. Our

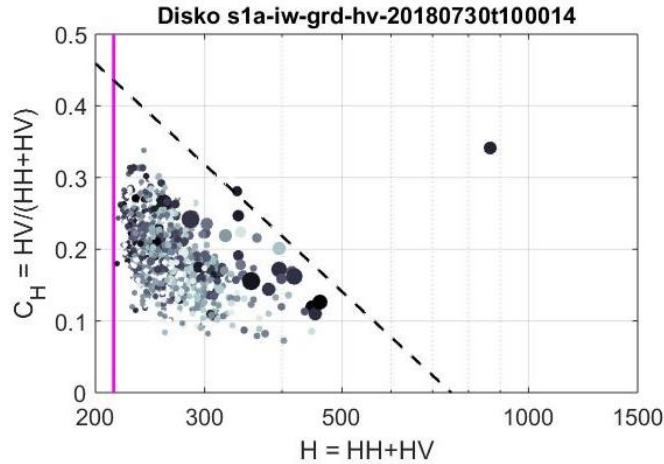detection and classification algorithm finds almost all ships recorded by AIS.

Fig. 4. Scatter plots of all segments (mainly icebergs) found in the Disko Bay ROI of Fig.1. Backscatter distribution C_H vs. $\bar{H}$, where size is proportional to area A and shading to B/L. This gives a visual view of the four classification parameters. Vertical line is the threshold T_B. Almost one thousand icebergs and ice floes are correctly classified below the dashed line. According to AIS there are two ships present of which the large cruise ship Ocean Diamond is clearly separated on the right whereas a smaller trawler is not identified.

As described in [12-13], one can for each object calculate the center of mass coordinates, length (L), width or breadth (B), orientation angle as well as a number of other spatial parameters for the segment. In the multispectral S2 images, these parameters were exploited for spatial classification of the segments as objects as ships are elongated and generally have small breadth to length ratio, B/L. As will be discussed in Sec. IV, the S1 IW SAR images have poorer resolution 20x22m. Also ship wakes are fragmented and not nearly as visible as for the S2 multispectral ship wakes. We therefore find that B/L is not as useful for a ship classification parameter for S1 images.
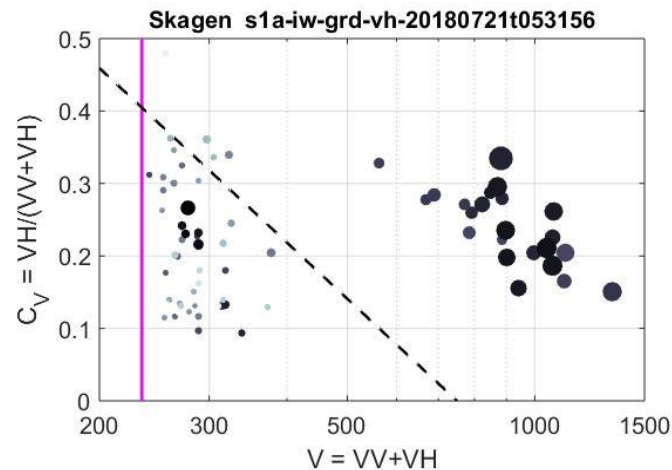

Fig. 5. As Fig. 4 but for all segments (mainly ships, sidelobes and wakes) found in Fig. 2 of Skagen. Dashed line is the k-nearest-neighbor (kNN) classification decision boundary.

The remaining classification possibilities are the two backscatter polarizations. We find that the average object backscatter $\bar{V}$ and the cross polarization C_V are good classifiers as shown in Fig. 5. Ships reflect much stronger than wakes and ice floes, i.e. their radar cross sections are much larger due to metal and flat surfaces and possible corner reflectors, in particular for VH. Therefore large ships show up on the right in Fig. 5, whereas wakes, sidelobe segments and unfortunately also some small ships show up on the left.

In Fig. 2 ships are denoted white numbers, whereas objects classified as wakes, sidelobes, harbor quay and a few small ships are denoted other colors. This allows for a quick identification of objects in the images with reference to the identification list with position, size, size after sidelobe correction, length, breadth, orientation, backscatter, etc.

C. Islands, sea turbines, oil rigs

Stationary objects such as islands and wind turbines are separated by change detection. By comparing to earlier S1 image(s) of the same region, and checking whether an object was present at the same place within a few pixels, we can remove most stationary objects as islands, sea turbines, oil rigs, harbor quays, etc. We choose a 5 pixel radius corresponding to 50m, which is large enough to be robust towards noise and some change in backscatter with time, but small enough that accidental position overlap between two moving objects is improbable.

D. Classification Accuracy and Comparison to AIS

The above object classifications indicate that the backscatter parameters $\bar{H}$ or $\bar{V}$ and C are much more useful than spatial classification parameters A and B/L when it comes to discriminating ships from icebergs in S1 IW images. As shown in Fig. 5+6 large ships and icebergs can to a large degree be separated in both $\bar{H}$ vs C_H and $\bar{V}$ vs. C_V plots by the dashed line.

Smaller ships and boats as well as sidelobes and wakes, however, tend to be widely spread into the iceberg classification region - leading to mis-identification. These results for S1 SAR ship and iceberg classification are compatible with earlier analyses based on dual cross polarisations from RadarSAT, TerraSAR and other satellite data [2].

Note that almost all the Arctic S1 IW images are HH whereas non-Arctic are VV, which complicates the classification because there are few ships in HH and few icebergs in VV. We therefore use the same dashed line for classification in Figs. 4+5 for lack of data. A differentiated classification should exploit that the sea background has more than double reflection in VV than HH. This will, however, require more ships with AIS records in the Arctic and records of icebergs drifting south.

Santamaria et al. [9] have analyzed more than two thousand S1 extra wide swath (EW) images with 50x50m resolution in the Arctic in which they have detected 13,312 objects all believed to be ships. On average 84% of these were correlated to AIS ships. The detection probability was 80-100% for ship lengths above 150m but dropped to 60-70% for ship lengths around the S1 EW resolution of 90m, and below 20% for ships shorter than 20m. This gave an average detection of 52% of the AIS ships in the S1 EW images.

We have performed a similar analysis for about 30 S1 IW images which contain about 200 ships in total. Although our statistics are limited, the about 5 times better resolution in the IW than EW images clearly improves the detection probability of large ships. We find almost 100% correlation between S1 IW and AIS for ships longer than 100m. For smaller ships, however, the detection probability drops rapidly to zero as for S1 EW.

For comparison, the high resolution multispectral S2 images had a detection probability of almost 100% even for small ships of length 20m [12-13]. Also, a greater number of small ships were detected which did not transmit AIS, probably because AIS reporting is only required by law for ships above 25m.

IV. SHIP LENGTHS AND WIDTHS

For each connected segment in the images we can calculate its position, heading angle, length and breadth as described in detail in the ship model algorithm of [12]. The image processing techniques are general and apply to both S1 and S2 images. However, the different backgrounds, noise, speckle and resolution affect the results. The resulting ship lengths and breadths are plotted in Figs. 6+7 vs. their ground truth values as given by AIS. We find that it is important to correct for sidelobes as they corrupt the ship images considerably and result in erroneous ship orientations, exaggerated lengths and breadths. The sidelobe corrected ship lengths and breadths from S1 data are closer to the ground truth numbers from AIS. The S1 ship lengths and breadths do, however, overestimate the ground truth dimensions by a constant offset of 36m and 26m respectively as shown in Fig. 6+7. The discrepancy is due to the limited S1 GRDH resolution of 20x22m and less importantly the pixel resolution of 10m. Correcting for this off-set, the standard deviation σ defined as the root mean square average of the difference between the S1 satellite data and the AIS ground truth ($L_{S1} + B/2 - L_{GT}$) is σ = 24m for the ship lengths and $\sigma(B_{S1} - B_{GT}) = 9m$ for the ship breadths. Note that one can observe the effect of the ship sterns which extends the ship length by of order half the ship width as explained in [12].

In Fig.6+7 the S2 optical data ship lengths and breadths from [12] are also shown for comparison. These agree much better with ground truth AIS values because the resolution is only the pixel length l=10m and there are four high resolution

bands. Also the background noise is less and no sidelobes are present. The resulting standard deviations were σ(L_{S2}+B/2 − L_{GT}) = 10 m and σ($B_{S2} − B_{GT}$) = 4 m and a very small offset of order 2m between S2 and AIS ship lengths and breadths.

As described above the ship images are corrected for sidelobes, and the resulting ship lengths and breadths calculated depend on the parameters $(S_0, \lambda_i, \lambda_j)$. The stronger the correction, the smaller the length and width, but at the same time the off-set decreases. The resulting offset corrected ship lengths and breadths are found to be robust, i.e. almost independent of the sidelobe parameters within a reasonable range around the parameters chosen.
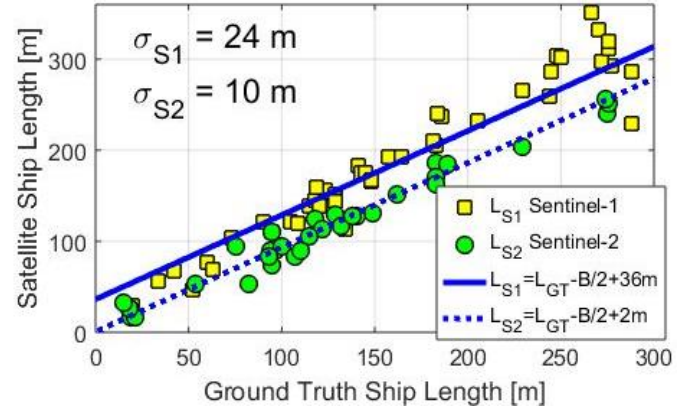

Fig. 6. Ship lengths. Squares and circles are from S1 and S2 data respectively vs ground truth lengths and breadths from AIS ship records. Blue lines indicate best off-set fit to S1 data and dashed blue line to S2 data, see text.
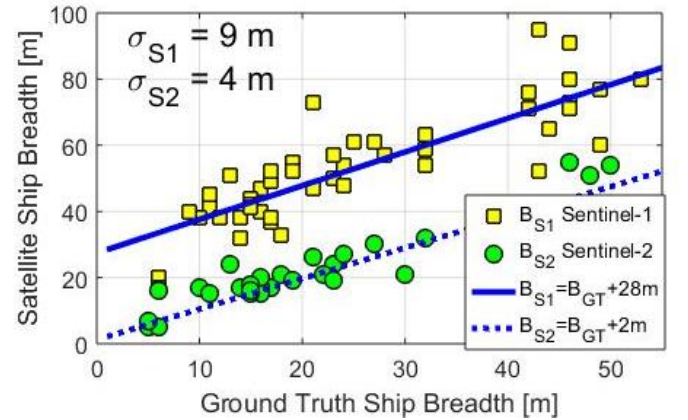

Fig. 7. As Fig. 6 but for ship breadths.

V. COMPARISON TO OTHER WORK AND CONCLUSION

Brusch et al. [5] have performed a similar analysis of ship lengths for TerraSAR satellite images, which have resolution down to 3-4m. They find a good linear correlation for ship lengths between 50-300m with a standard deviation of 22m and an offset (negative bias) of 7m. The offset is smaller due to the better resolution as could be expected, and is comparable to the resolution as is also the case for our Sentinel-1 data.

Surprisingly, the standard deviation in TerraSAR ship lengths is much larger than the resolution and comparable to that found in the S1 analysis above. Part of the reason could be the sidelobe reduction performed on the S1 data. We also suspect that the higher detail in TerraSAR resolves high and low reflective parts of the ships, which complicates the spatial analysis and dimension determination. Therefore, the S1 images are useful for ship detection and they also cover larger areas and thus allow for faster wide area search.

Bentes et al. [4] have analyzed a wide range of TerraSAR-X modes and found relations between resolution and minimum ship length detection. At wide incidence angle and low wind speed they are similar, but at low incidence angle and/or higher wind speed the large backscatter from the sea makes detection more difficult and the minimum detection length can increase by an order of magnitude compared to the resolution. Extrapolating to the resolution and inclination angles in our S2 data, we find that our ship length off-set and standard deviation are compatible with their ship size detectability lengths.

Stasolla and Greidanus [10] have analysed 127 ships in S1 GRDH images from the Panama Canal. Their method exploits the topology information of the ship backscatter geometry to place a rectangle for ship length and width estimates. Their methodology avoids an off-set. Comparing to AIS data they find an absolute error of 30m and 11m respectively. Both are compatible with the standard deviations found in this analysis.

Hajduch et al. [11] analyse a large number of ships in Envisat ASAR/WSM/VV images. Besides geometrical information they also exploit the ship normalized radar cross section to improve their ship length and width estimates. Their methodology seems to remove off-set lengths. A comparison to AIS data shown in a plot seems to have a variation as in Fig. 7 but no standard deviation is given.

VI. Summary

Sentinel-1 SAR data was analyzed in detail including search and detection of objects above sea background with masking of land and sea ice. An algorithm for suppressing sidelobes from strongly reflecting objects such as large ships was found very useful for determining ship lengths and breadths more accurately. As result good comparison to AIS ground truth numbers was found, however, with a large offset of around 30m due to the corresponding resolution of the S1 data. The standard deviation between ship lengths from AIS and satellite data was of similar size 24m and surprisingly similar to earlier TerraSAR-X [5] analyses although this data has much better resolution. In comparison Sentinel-2 multispectral analysis could determine ship lengths and breadths much better [12].

For classification a change detection algorithm proved very useful for identifying stationary objects such as sea turbines, islands, piers, etc. by comparing object positions from different satellite overpass. This simplified the classification of the remaining changing objects such as ships and icebergs.

However, it was found that for the S1 SAR data as opposed to S2 multispectral data [13], the spatial information such as area, length and width was not very useful for classifying ships in Greenland when icebergs are abundant because they can have very different form and sizes and the resolution is limited. Instead, the average and cross radar polarization backscatter were significantly larger for large ships and allowed for correct classification of large ships vs. icebergs using a simple k-nearest-neighbor method. However, smaller ships and wakes proved very difficult to separate from icebergs.

Neural networks show promising results for discriminating smaller ships from icebergs [14-15]. Correlating to AIS data will be important for better determination of true/false positive/negative alarms, and finding *dark ships*. The detection of ships vs. icebergs in all weather day and night SAR data will be useful in ice infested arctic seas for surveillance, monitoring navigation, rescue service, etc.

References

[1] ESA Copenernicus Program, Sentinel Scientific Data Hub. https://sentinel.esa.int/web/sentinel/user-guides/sentinel-1-sar/document-library/-/asset_publisher/1dO7RF5fJMbd/content/sentinel-1-product-definition

[2] C-CORE. "Summary of previous research in iceberg and ship detection and discrimination in SAR," *DRDC report no: R-13-060-1098*, 2013.

[3] G. Saur, M. Teutsch, "SAR signature analysis for TerraSAR-X-based ship monitoring," *Image and Signal Processing for Remote sensing XVI. Proc. of SPIE* Vol. 7830, pp. 78301O-1, 2010.

[4] C. Bentes, D. Velotto, S. Lehner, "Analysis of ship size detectability over different TerraSAR-X modes," *IGARSS IEEE*, pp. 5137, 2014.

[5] S. Brusch, S. Lehner, T. Fritz, M. Soccorsi, A. Soloviev, B.v. Schie, "Ship surveillance with TerraSAR-X," *IEEE Transactions on Geoscience and Remote Sensing*, 2010.

[6] S. Brusch, S. Lehner, E. Schwarz, T. Fritz, "Near real time ship detection experiments," *Proc. SeaSAR 2010,* Frascati. ESA SP-679, 2010.

[7] D. Velotto, M. Migliaccio, S. Lehner, "Dual-Polarimetric TerraSAR-X SAR data for target at sea observation," *IEEE Geoscience and Remote Sensing Letters*, Vol. 10, p. 1114, 2013.

[8] C. Brekke, D.J. Weydahl, Ø. Helleren, R. Olsen, "Ship traffic monitoring using multipolarisation satellite SAR images combined with AIS reports," *Proc. of the 7th European Conference on Synthetic Aperture Radar (EUSAR)*, Friedrichshafen, Germany, 2–5 June, 2008.

[9] C. Santamaria, H. Greidanus, M. Fournier, T. Eriksen, M. Vespe, M. Alvarez, V.F. Arguedas, C. Delaney, P. Argentieri, "Sentinel-1 contribution to monitoring maritime activity in the Arctic," *Proc. Living Planet Symposium 2016*, Prague, ESA SP-740, 2016.

[10] M. Stasolla, H. Greidanus, "The exploitation of Sentinel-1 images for vessel size estimation," *Remote Sens. Lett.,* vol. 7, no. 12, pp. 1219-1228, 2016

[11] G. Hajduch, N. Longepe, J. Hanonneau, J.Y. Le Bras, "Progress in automatic ship detection and classification," *Proc. SEASAR 2012*, Tromso, Norway, 2012, ESA SP-709 2013, id. 19

[12] H. Heiselberg, "A direct and fast methodology for ship recognition in Sentinel-2 multispectral imagery by supervised classification," *Remote Sens.*, vol. *8*, pp. 1033, 2016. https://doi.org/10.3390/rs8121033

[13] P. Heiselberg, H. Heiselberg, "Ship-Iceberg discrimination in Sentinel-2 multispectral imagery," *Remote Sens.*, vol. *9*(11), pp. 1156, 2017. https://doi.org/10.3390/rs9111156

[14] C. Bentes, A. Frost, D. Velotto, B. Tings, "Ship-Iceberg discrimination with convolutional neural networks in high resolution SAR images," *Proc. of EUSAR*, 2016.

[15] Iceberg Classifier Challenge 2018 in Machine Learning, https://www.kaggle.com/c/statoil-iceberg-classifier-challenge